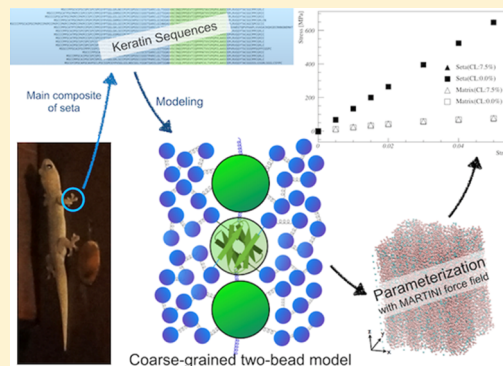


Coarse-Grained Molecular Simulation Model for Gecko Feet Keratin

Kenkoh S. Endoh,^{*,†,‡} Toshihiro Kawakatsu,[‡] and Florian Müller-Plathe[†][†]Eduard-Zintl-Institut für Anorganische und Physikalische Chemie, Technische Universität Darmstadt, Alarich-Weiss-Street 8, D-64287 Darmstadt, Germany[‡]Department of Physics, Tohoku University, Aramaki Aza Aoba 6-3, Aoba-ku, 980-8578 Sendai, Japan

ABSTRACT: The mechanical properties of gecko setae and spatulae are investigated with a coarse-grained model having two bead types. The two-bead model is based on both experimental information of the internal structure of setae and the chemical amino acid composition. Because the seta is composed of a stiff fibril region and a soft matrix region, we model each of the regions separately. Our model is parameterized in a bottom-up way, and it successfully predicts essential mechanical properties without optimization against the macroscopic properties of keratin. Young's modulus of the fibril area (13.2 ± 0.02 GPa) is 6 times stiffer than that of the pure matrix (2.13 ± 0.059 GPa). Because the volume fraction of the matrix decreases toward the top of a seta, its distal area should be stiffer than its proximal area. The anisotropy of the fibrils is clearly confirmed by the comparison between Young's modulus and the shear modulus of the fibril region. Our model also lends some support to the notion that water uptake selectively weakens the axial cohesion of the fibrils, which leads to the experimentally observed plateau in the stress–strain curves beyond 2% strain for setae under high relative humidity.



1. INTRODUCTION

Geckos, insects, and spiders have the ability to cling to and walk on walls and ceilings without the need for an auxiliary adhesive. This phenomenon, called dry adhesion, and its mechanism have been under intense investigation.^{1–3} Although the architecture of gecko toe pads and its action is well understood from the macroscopic down to the micrometer level, relatively little is known about the role of the base material, β -keratin, at the molecular scale. On each toe pad, there are millions of fibers called setae, which are of micrometer size. At their ends, each branches into hundreds of spatulae,^{4–6} which are several hundreds of nanometers wide (schematically shown in Figure 1A). Setae are composed of stiff fibril regions embedded in a soft matrix (Figure 1B). The volume fraction of the matrix region decreases toward the tip, and spatulae consist mainly of fibril region.^{4,7} It has been suggested that spatulae interact with any kind of surface through van der Waals forces.⁸ This interaction is enabled by not only the above fine structure of the toe pads but also the chemical composition of the spatula and the mechanical properties of the keratin.^{5,9,10} In this study, we construct a mesoscale two-component model that represents both setae and spatulae, with a focus on the mechanical properties and their relation to molecular structure.

The mechanical properties of setae and spatulae have been measured experimentally under different relative humidities (RH). Young's moduli of a seta in fibril direction have the following values: 7.3 ± 1.0 GPa in vacuum,⁷ 3.7 ± 0.1 GPa at 30% RH,¹¹ and 2.13 ± 0.2 at 80% RH.¹¹ Water molecules

soften setae and cause a plateau in the stress–strain curve between 2 and 8% elongation.¹¹

There have been several theoretical investigations^{2,10,12–14} to clarify the relationships between mechanical properties and adhesion on the macroscopic and biological length scales (>0.1 μm). The theories account for the forked structure of seta and spatula and mimic the structure by simple springs¹² or more realistic elastic models.¹³ As the mechanical properties affect the adhesion on the macroscopic scale, the stiffness is one parameter determining the adhesion in these models. Experimental values have been used for this purpose.^{10,12,13} In contrast, no molecular models capable of predicting the elasticity and its anisotropy for β -keratin have been put forward. Avian feathers have a similar internal structure. Their Young's modulus is 2.50 ± 0.064 GPa at ambient humidity.¹⁵ There has been more theoretical research on α -keratin-based human hair and other mammalian fibers,^{16–19} partly because these materials have commercial importance as targets for body care products. There has been a two-phase continuum model for its mechanical properties,¹⁶ from which a mesoscopic molecular coarse-grained model has been constructed as an extension of the two-phase model.¹⁷

In this study, we construct and test a particle-based mesoscale model of β -keratin for molecular simulation. It consists of different types of beads for the two components, which form the internal structure of setae and spatulae. It

Received: October 23, 2017

Revised: January 18, 2018

Published: February 1, 2018



contains stiff units for the fibrils and more flexible units for the surrounding amorphous matrix.^{16,17} The molecular interactions are modeled in a bottom-up manner using the chemical composition of β -keratin. We note that no macroscopic elasticity information has been used in the construction of the model. As the experimental data are not available for the gecko, we supplement them with information for other species with similar properties. We discuss the role of the internal morphology of setae and spatulae within this model, focusing on the mechanical properties, and discuss the experimental behavior of seta from microscopic level.

2. MODEL CONSTRUCTION

The keratin in setae consists of stiff fibrils (FB, dark areas in Figure 1B) in a soft matrix (MX, light areas in Figure 1B). Cross-sectional micrographs have clarified that the fibrillar regions extend continuously from the bottom of a seta into the spatula^{4,7} and that fibrils are the main building blocks of the fiber structure. According to the comparison of keratin amino acid sequences between gecko setae and bird feathers,^{20–22} X-ray scattering data for both materials,^{4,23} and micrographs of the fine structure in feathers,²⁴ the fibrillar area contains both microfibrils and matrix material (Figure 1C). In contrast, pure matrix regions in Figure 1B are found only between the bottom and the middle of the seta (FB + MX region in Figure 1A) and their volume fraction decreases toward the branching area.

The dominant chemical constituents of setae, especially in the fibril region, are β -keratin.^{4,20} An immunocytochemical measurement shows that setae are made up of cysteine-rich keratins.²⁰ Although the existence of α -keratins in seta has been discussed,^{4,20,25} X-ray diffraction shows only the β -sheet pattern.⁴ Thus, if α -keratins exist in setae, their concentration must be low. On the other hand, the material of the matrix region has not yet been identified completely and there are a few candidates: protein matrix¹¹ or lipids.²⁶ We assume that the matrix region is made from a protein, whose internal structure is isotropic and disordered. As the fibril area also contains matrix regions, we concentrate on the discussion of the fibril region.

A total of 16 cysteine-rich keratins (Ge-cprp-1 to 16²⁷) have been sequenced. All sequences show three segments with different secondary structures:^{21,22,27} random coil, β -sheet, and random coil regions from the head to the tail. The random coil segments do not take any defined conformation and form the amorphous matrix. In contrast, the β -sheet region is made from 32 residues called core-box and R-box by Alibardi et al.^{21,22,25,27} Their β -sheet structures have been confirmed by X-ray diffraction.¹¹ A comparison of keratin sequences between setae and avian feathers also supports the existence of a β -sheet region.^{11,21,23} A higher-order structure is known for avian feathers,^{21–23} in which β -sheets dimerize (Figure 1D) to form a section of a microfibril in the fibril area (Figure 1C). The dimer has a helical structure, and each dimer extends 2.4 nm in the fibril direction.^{22,23} As a dimer rotates by ca. 90° from one end to the other, four dimers are required to complete a full turn. Interestingly, the sequence of the cysteine-rich keratins leads to the presence of both the fibril proper and amorphous matrix material in the fibril region (Figure 1C).

We construct a two-component model for seta's fibril region (Figure 1E, left). Because there is no specific structure in random coil sequences, the conformational degrees of freedom become important in this region. We set the size of a matrix (MX in Figure 1E, left) bead to be that of an entire amino acid

and ignore anisotropies from amino acid side groups. The mass of an MX bead (96.65 g mol⁻¹) is the average over all residues according to their proportion. The head region is made from 64 MX beads, whereas 23 MX beads represent the tail region. In contrast, a β -sheet dimer is rigid and each amino acid only vibrates around its equilibrium position. Because the covalent bond between β -pleats (intradimer interaction) is much stronger than the interdimer interaction, we ignore the deformation and disaggregation of dimers in our model. Therefore, one β -sheet dimer is represented by a single, big fibril (FB in Figure 1E, left) particle encompassing 64 amino acids (two β sheets in Figure 1E, left). The mass of an FB bead is 6.374 kg mol⁻¹. In our model, two head and tail regions, namely, 4 MX branches (2 short, 2 long) are attached to every FB bead (Figure 1E, left).

A fibril modeled in this way is of a pearl-necklace form (Figure 1E, left). In contrast, a real dimer takes a blocklike form, whose flat surfaces strongly interact with adjacent dimers. Hence, a fibril takes a cylindrical shape rather than a series of spherical interaction sites. Our unrefined pearl-necklace representation would have space for small MX beads to unrealistically penetrate between FB beads when an elongation deformation is imposed on the system. To prevent the spurious penetration and to better approximate the cylindrical shape, we add an additional bead between two neighboring FB beads (Figure 1E, right). We set identical parameters, such as the diameter, mass, and interaction, for the original FB bead and the additional bead. Under this condition, the mass of FB bead becomes half of the original value (3.187 kg mol⁻¹) to keep the density of the system. The interaction parameters, especially the bonded interaction, are modified to keep the same pressure and stress even when we place the additional beads in the system because our target is the mechanical properties that strongly relate to the stress tensor. Details of the model parameters, such as bonded interaction, excluded volume, and strength of nonbonded interaction, will be discussed in the Parameterization section below. Because both the original FB bead and the additional bead have identical properties, we refer both of them as FB beads. When we explicitly mention the original FB bead, for instance, indicating an FB bead connecting to MX beads, we indicate it with prime (FB').

The alignment of the fibrils in setae has not been completely clarified yet because the resolution of existing micrographs is too low to quantify it.^{4,7,20,26} However, an image of an avian feather (Figure 10 in ref 24) helps to make a reasonable assumption about the alignment. The cross-sectional picture shows the matrix and highly ordered fibril areas. The fibrils are hexagonally arranged, which is also confirmed by their two-dimensional radial distribution function. We, therefore, adopt a hexagonal packing of parallel fibrils also in our model of gecko setae. If we use a rectangular unit cell and set the direction of fibril in z , the cross section of the seta corresponds to the xy plane. The ratio of the unit cell dimensions in x to y is $L_y/L_x = \sqrt{3}$. With a typical keratin density of 1.3 g cm⁻³,^{23,28} and setting the length of z direction to be the pitch of the full helix turn (4×2.4 nm = 9.6 nm), we estimate the Cartesian dimensions of a rectangular unit cell to be $3.78 \times 6.55 \times 9.6$ nm³.

3. PARAMETERIZATIONS

We used the coarse-grained MARTINI force field as a starting point of our parameterization because it is available for all

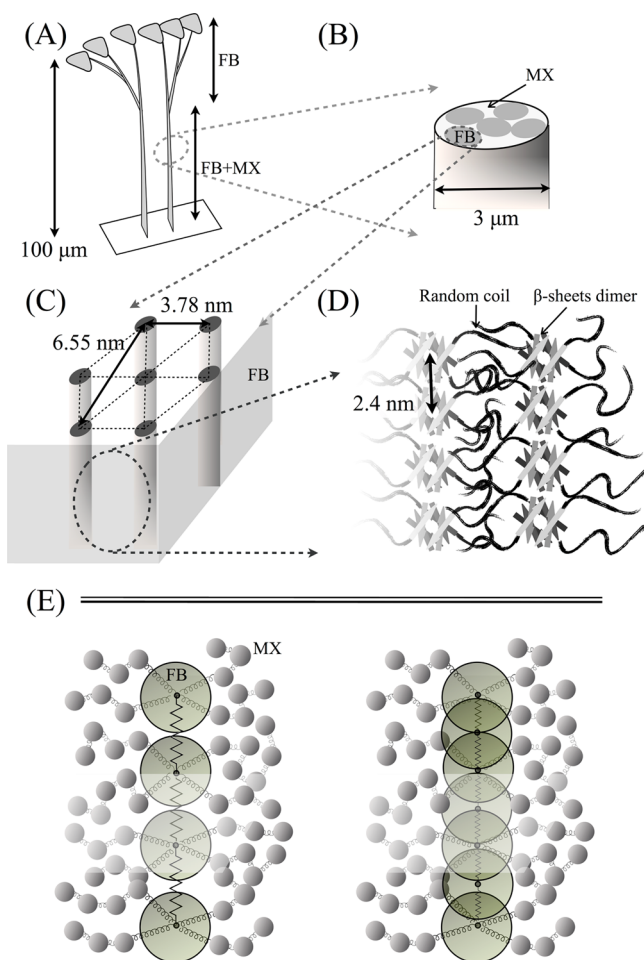


Figure 1. Schematic pictures of a gecko seta. (A) Setae measure 100 μm in longitudinal direction. Spatulae and setae are mainly made from β -keratins. (B) The cross section of the setae has a diameter of 3 μm ,⁴ and soft matrix (ca. 30%⁷) and fibril regions are found. According to the micrographs, material on the surface of seta is the same as in the fibril region. (C) Internal structure of the fibril region of (B) (assumption). It is made of nanofibrils and an amorphous matrix. The X-ray diffraction patterns and the comparison of keratin sequences between seta and avian feathers support this configuration. The nanofibrils are aligned in a hexagonal packing with a distance of 3.78 nm on xy plane. (D) Dimers of β -keratin construct a fibril, whose diameter is almost 2.4 nm, and matrix area simultaneously. A β -sheet region is found at the center of each keratin sequence (described in arrows), whereas the tail ends form the amorphous matrix area. (E) Left: coarse-grained model of the keratin dimers. A dimer of β -sheets is represented by a big bead because the dimer does not change its conformation. In contrast, an amino acid in matrix area is expressed by a small bead and the series of the small beads takes flexible conformation. Right: the additional big beads are inserted for small beads not to penetrate between the big beads.

amino acids^{29–31} and yields reasonable mechanical properties compared to experiment.³²

Bonded harmonic potentials between MX beads are taken from the original values of the MARTINI force field:^{30,31} the equilibrium distance $r_b^{\text{MX-MX}} = 0.35$ nm and the force constant $k_b^{\text{MX-MX}} = 1250$ kJ mol^{−1} nm^{−2}. The angle potentials are also taken from the original values:³¹ the equilibrium angle $\theta^{\text{MX-MX-MX}} = 127^\circ$ and the force constant $k_a^{\text{MX-MX-MX}} = 20$ kJ mol^{−1}.

The interaction among consecutive FB' beads is tricky because one FB' bead represents an entire dimer of β -sheets. The equilibrium distance between two FB' beads in fibril direction ($r^{\text{FB'-FB'}} = 2.4$ nm) is taken from X-ray diffraction data.^{21,23} Physically, the FB'–FB' interaction is a very strong nonbonded interaction between the surfaces of β -sheets. It is so strong that we may replace it with a bonded potential. To come up with interaction parameters for it, first, all residues of an FB' bead are placed on the coordinates of β -sheets [Table 2 in ref 23]. Next, we put two dimers with the equilibrium distance (2.4 nm) apart. Then, we evaluate the potential energy by changing the distance between the two surfaces or tilting the angle between the two surfaces. Finally, we convert the numerical table of potentials into a bond and an angle potential. From the fitting of the numerical potential with Lennard-Jones (LJ) 12-6 interaction, we get strength of the potential $\epsilon^{\text{FB'-FB'}} = 134.2$ kJ mol^{−1} and effective bead diameter $\sigma^{\text{FB'}} = 0.456$ nm: only surface amino acids interact, and the diameter is close to the effective diameter of a single amino acid. The potential is shifted by $r_0 = 1.889$ nm outward to set the most stable point at the equilibrium distance ($r^{\text{FB'-FB'}} = 2.4$ nm). From the curvature of the LJ potential at the equilibrium distance ($r = 2^{1/6}\sigma$), we derive a harmonic force constant

$$k_b^{\text{FB'-FB'}} = \frac{72}{2^{1/3}} \frac{\epsilon^{\text{FB'-FB'}}}{\sigma^{\text{FB'}^2}} = 57.146 \frac{\epsilon^{\text{FB'-FB'}}}{\sigma^{\text{FB'}^2}}$$

which leads to $k_b^{\text{FB'-FB'}} = 3.688 \times 10^4$ kJ mol^{−1} nm². Now, the strength of the bonded interaction between FB' beads is converted to FB–FB interaction. The number of total FB beads is twice that of FB' beads in a fibril, and the pressure must be kept the same upon the insertion of additional beads as described above. By considering the combination rule of springs in series, the interaction strength should be twice the original value: $k_b^{\text{FB-FB}} = 2k_b^{\text{FB'-FB'}} = 7.38 \times 10^4$ kJ mol^{−1} nm². Consequently, the bonded potential becomes $V_{\text{bond}} = (k_b^{\text{FB-FB}}/2)(r - r_b^{\text{FB-FB}})^2$, where $r_b^{\text{FB-FB}} = r_b^{\text{FB'-FB'}}/2 = 1.2$ nm.

We express the potential energy due to the tilt of dimers as a quadratic form around the equilibrium angle ($=0^\circ$). This potential is converted from the tilt angle between surfaces of β -sheets to a three-body bond–angle interaction between subsequent FB beads. For small tilts, there is little angle dependence of the potential. We approximate this region by a quadratic form $V_{\text{angle}} = (k_a/2)(\theta - \theta^{\text{FB-FB-FB}})^2$ with the parameters $\theta^{\text{FB-FB-FB}} = 180^\circ$ and $k_a^{\text{FB-FB-FB}} = 0.68$ kJ mol^{−1} deg^{−2}.

Finally, the four MX chains dangling from each FB' bead are distributed equally around it. In this conformational arrangement, the terminal 4 MX beads (2 beads for short chains and other 2 beads for long chains) are connected to an FB' bead in a plane vertical to the fibril ($\theta_a^{\text{FB-FB'-MX}} = 90^\circ$). The angle formed by MX–FB'–MX beads in the plane is equally arranged ($\theta_a^{\text{MX-FB'-MX}} = 360^\circ/4 = 90^\circ$). To keep the angular geometry among MX and FB beads, we use a strong angle potential $k_a^{\text{FB-FB'-MX}} = k_a^{\text{MX-FB'-MX}} = 100$ kJ mol^{−1} with the form of $V_a = (k_a/2)(\cos \theta - \cos \theta_a)^2$. The equilibrium distance is the arithmetic mean of both bonds: $r_b^{\text{FB'-MX}} = (0.35 + 2.4)/2 = 1.375$ nm, whereas the strength is the same as the MX–MX interaction ($k_b^{\text{FB'-MX}} = 1250$ kJ mol^{−1} nm^{−2}) because MX and FB' are connected by the same kind of covalent bond as in the original force field. The angle potential of MX beads from an FB' bead (FB'–MX–MX) is also taken from that of MX

Table 1. Summary of Bonded Interactions^a

bonds	r_b [nm]	k_b [kJ mol ⁻¹ nm ⁻²]	bond angles	θ_a [deg]	k_a
MX–MX	0.35	1250	MX–MX–MX, FB–MX–MX	127	20 [kJ mol ⁻¹]
FB–FB	1.2	7.38×10^4	FB–FB–FB	180	0.68 [kJ mol ⁻¹ deg ⁻²]
MX–FB	1.375	1250	FB–FB–MX, MX–FB–MX	90 (and 180)	100 [kJ mol ⁻¹]

^aMatrix beads are denoted by MX and fibril (β -sheet dimer) beads as FB.

beads: $\theta_{\text{FB–MX–MX}} = 127^\circ$ and $k_a^{\text{FB–MX–MX}} = 20 \text{ kJ mol}^{-1}$. The parameters for bonded potentials are listed in Table 1.

The gecko β -keratin contains many cysteine residues. Their thiol groups are likely oxidized to disulfide bonds, which cross-link (CL) different protein chains. The cross-links not only provide extra structural integrity to the keratin, but also, in polymer language, turn it from a melt into an elastomer. In gecko keratin, 17.7% of the amino acids are on average cysteine. Therefore, for all 100 amino acids, statistically 8.9 cross-links are possible, which we denote in shorthand as 8.9%. For gecko setae, the number of possible disulfide bonds realized is not known. There is, however, information on the cross-link for the β -keratin of avian feathers ($9.0 \pm 1.7\%$ ³³) and tortoise shells ($7.4 \pm 0.57\%$ ³³). We, therefore, decided to use a similar cross-link density of 7.5% in our keratin model and connected MX beads randomly. We use the same bonded harmonic potential as for the bonds within one keratin molecule ($l_b = 0.35 \text{ nm}$ and $k_b = 1250 \text{ kJ mol}^{-1} \text{ nm}^{-2}$).

Nonbonded interactions are modeled with the Lennard-Jones 12-6 potential. Our model has one MX bead type and one FB bead type, where we do not distinguish the difference between the amino acids. Therefore, the interaction parameters ϵ and the bead diameters σ must reflect the average properties of amino acids for the composition at hand. We start from the ϵ of the MARTINI force field. Because it represents each amino acid by between one and five beads,³⁰ we need to convert the interaction parameter ϵ of MARTINI force field into interaction parameters for our condensed MX and FB beads. The following combination rules account for the amino acid ratio in the seta, the secondary structure, and the geometry of the dimer.

First, the interaction parameters of the MARTINI beads of each amino acid^{29,30} are simply added and an interaction table for each pair of amino acids is compiled. These terms do not include any geometrical effect between backbone and side groups and therefore these parameters overestimate the interactions. Second, we average the strength according to the statistical occurrence of each pair of amino acids in keratins, which we calculate as an average of all cysteine-rich keratins in seta²⁰

$$\epsilon' = \sum_{\text{all combinations } mn} \frac{N_{mn}}{N} \epsilon_{mn}$$

where N_{mn} is the number of possible pairs of amino acid types m and n , N is the total number of pairs, and ϵ_{mn} is the interaction strength between amino acids m and n . For example, if the matrix is composed of 10 prolines (P) and 5 cysteines (C), we calculate $N_{PP} = 10 \times (10 - 1)/2 = 45$, $N_{CC} = 5 \times (5 - 1)/2 = 10$, $N_{PC} = 10 \times 5 = 50$, and $N = N_{PP} + N_{CC} + N_{PC} = 105$. With $\epsilon_{PP} = 12.9$, $\epsilon_{CC} = 15.3$, and $\epsilon_{PC} = 13.9 \text{ kJ mol}^{-1}$, the appropriate interaction parameter becomes $\epsilon' = 13.6 \text{ kJ mol}^{-1}$. For the keratin studied here, we arrive at an averaged parameter of $\epsilon'^{\text{MX–MX}} = 14.8 \text{ kJ mol}^{-1}$ for the interaction between matrix amino acids (MX–MX) and

$\epsilon'^{\text{FB–MX}} = 14.4 \text{ kJ mol}^{-1}$ for the interaction between outer surface of β -sheet amino acids and matrix amino acids.

Next, we approximate effects of residue geometry and secondary structure. The original MARTINI force field has backbone beads and a varying number of side group beads for every amino acid, so the interaction between two amino acids depends on their relative orientation. Our single-bead amino acid model neglects this, and simply adding up the original ϵ 's overestimates the attraction. We estimate the overestimation in each secondary structure to correct for it. The possible orientations are restricted by the secondary structure (Figure 2): all orientations of two beads are possible in random coils,

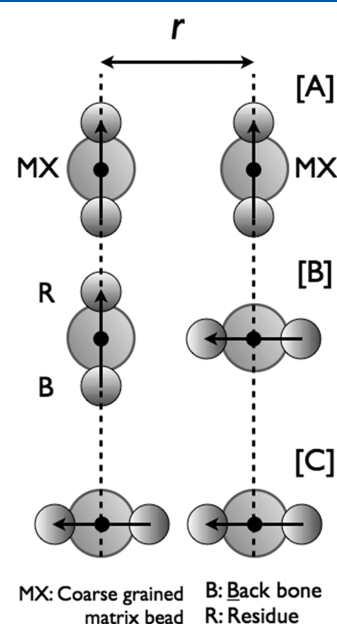


Figure 2. Typical orientation of two beads: a backbone (B) bead and a residue (R) bead at MARTINI force-field resolution. In contrast, coarse-grained matrix (MX) bead does not express any influence of orientations at MARTINI resolution. The amino acid takes several orientations according to the secondary structures. Normally, pattern [A] takes the highest energy, followed by patterns [B] and [C], and these differences read to the scaling factor.

types [B] and [C] are possible between β -sheet and random coil amino acids, and only type [A] is possible among amino acids on the turning points of the β -sheet surface between dimers.²³ As a simple example, if we count the contacts for the two-site MARTINI model (most residues) and assume for simplicity equal ϵ 's, then the configuration [A] has two closest (r) and two distant ($\sqrt{r^2 + a^2}$) interactions, where r represents the center-of-mass distance between two amino acids and a represents the distance from the backbone to the side group; configuration [B] has two $\sqrt{(r - a/2)^2 + (a/2)^2}$ and two $\sqrt{(r + a/2)^2 + (a/2)^2}$ distances, and configuration

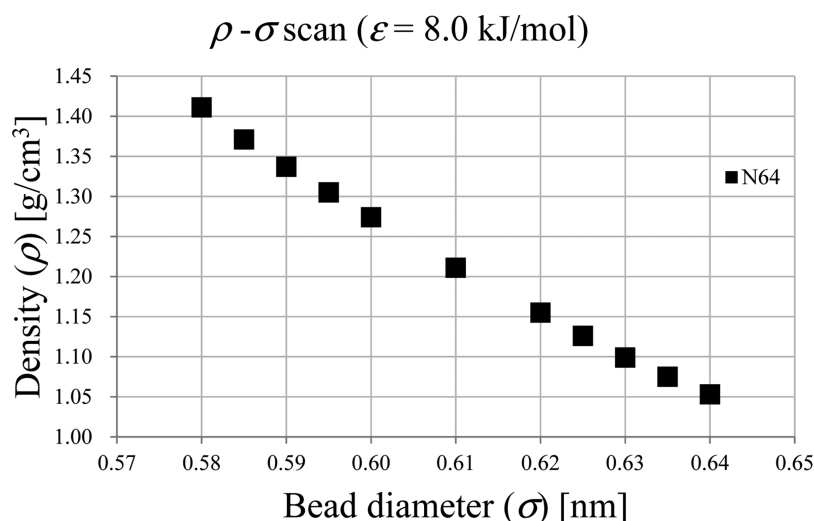


Figure 3. Relationship between density and the Lennard-Jones diameter σ of MX beads. The Lennard-Jones interaction strength is kept at $\epsilon = 8.0$ kJ mol⁻¹. The simulation was carried out with 64 linear polymer chains (N64), with each polymer containing 87 monomers. For further calculations, we adopt $\sigma_{\text{MX}} = 0.59$ nm. The results do not change if we carried out similar simulation with 25 molecules.

[C] has two r , one $r - a$ and one $r + a$. In contrast, the single-site model corresponds in strength to four equal interactions with distance r . Therefore, its strength must be rescaled to implicitly incorporate the effects of the other conformations. The scaling factor becomes 0.90 for configuration [A], 0.59 for configuration [B], and 0.35 for configuration [C]. We evaluate the scale factor for MX–MX as 0.54, MX–FB as 0.47, and FB–FB as 0.90. Through this procedure, we estimate our interaction parameter for the matrix beads to be $\epsilon^{\text{MX–MX}} = 8.0$ kJ mol⁻¹.

Finally, we consider the distribution of amino acids within a β -sheet dimer to obtain an improved nonbonded interaction between MX and FB beads and FB–FB interactions. We start with the backbone structure of β -sheets determined by X-ray diffraction.²³ We place an average amino acid on every backbone position. We then vary the position of a single MX bead around the β -sheet and find its minimum-energy position. The minimum energy $\epsilon^{\text{FB–MX}} = 28.6$ kJ mol⁻¹ is taken as the effective ϵ for the interaction between the MX and the entire FB bead. This procedure is similar in spirit to the parameterization between neighboring FB beads. The parameterization of nonbonded interaction between FB beads has been already discussed in the bonded potential, and it has been converted into a bonded potential. The scaling factor 0.90 to estimate the FB'–FB' interaction implies an ideal situation, where all residues on the surface of dimer align in parallel, and hence gives an upper limit of the interaction.

Next, we discuss the parameterization of the excluded-volume parameter σ^{MX} for matrix beads. We simulated a pure matrix system with 64 linear chains of 87 MX beads under constant temperature and pressure (NPT) conditions, with a time step of 12 fs, a Berendsen thermostat at 300 K with coupling times of 0.6 ps for temperature and 12.0 ps for pressure, and compressibility of 4.5×10^{-7} kPa⁻¹. The LJ diameter σ^{MX} of an MX bead is adjusted to the target density of general polymer (1.35 g cm⁻³).³⁴ The LJ interaction strength $\epsilon^{\text{MX–MX}}$ determined above is held at $\epsilon^{\text{MX–MX}} = 8.0$ kJ mol⁻¹, and the bead diameter σ^{MX} is varied between 0.58 and 0.64 nm. Figure 3 shows the relationship between σ and density. The density decreases monotonously with the excluded volume. An MX bead diameter of $\sigma^{\text{MX}} = 0.59$ nm must closely

reproduce the target density (1.34 g cm⁻³) of the matrix. We have also simulated pure matrix system with 27 linear chains or 125 linear chains and found that the dependence of system size is less than 2% in each bead diameter. We also simulated similar systems in MARTINI force-field resolution as a reference and found that the error of potential energy is less than 5% in all of system sizes.

The Lennard-Jones distance between MX and FB beads is estimated taking into account that the residues reside on the surface of a β -sheet. Because of the large size difference of the FB and MX beads, the use of the arithmetic mean of the two σ 's would lead to a wide potential well and a large cutoff. We rather use the σ of the MX beads but shift the singularity of the Lennard-Jones potential outward by $r_0^{\text{FB–MX}} = 0.8327$ nm. The modified Lennard-Jones potential thus is

$$V_{\text{LJ}}(r) = 4\epsilon \left[\left(\frac{\sigma^{\text{MX}}}{r - r_0^{\text{FB–MX}}} \right)^{12} - \left(\frac{\sigma^{\text{MX}}}{r - r_0^{\text{FB–MX}}} \right)^6 \right]$$

All parameters for the nonbonded potential are listed in Table 2. With this parameterization, the volume fraction of the FB beads in the seta model is about 36.6%.

Table 2. Nonbonded Interaction Parameters: Lennard-Jones Diameter (σ), Position of the Singularity (r_0), and Interaction Energy (ϵ)^a

nonbonds	σ [nm]	r_0 [nm]	ϵ [kJ mol ⁻¹]
MX–MX	0.59	0.0	8.0
MX–FB	0.59	0.8327	28.6

^aNonbonded interaction between FBs is converted to the bonded potential and is not nominated in the nonbonded interaction.

4. SIMULATION DETAILS

The simulation conditions are shown in Table 3. We simulate a seta model with FB and MX beads. The system size corresponds to the thickness of a spatula (ca. 20 nm in x and y directions). We account for the length of two helical loops (19.2 nm) in the direction of the fibril axis (z). The

Table 3. Simulated Systems^a

system	N_{molecule}	$N_{\text{atom/molecule}}$	$L_x L_y L_z$ [nm ³]
seta (FB + MX)	128	2 FB + (2 × 64 + 2 × 23) MX	15.485 × 13.411 × 19.20
pure matrix (MX)	125	87 MX	11.0 × 11.0 × 11.0

^a $N_{\text{molecules}}$ shows the number of molecules in a system. Each molecule is constructed from atoms listed in $N_{\text{atom/molecule}}$.

system contains 16 parallel fibrils of 16 FB beads each. Periodic boundary conditions are used in all Cartesian directions. For reference, we also simulate a pure matrix constructed from only MX beads. The size of the pure matrix system is (11.0 nm)³ with 125 linear chains of 87 MX beads, and it has cubic periodicity.

The molecular dynamics time step is 0.015 ps, and the system is annealed under NVT conditions (Berendsen thermostat with the coupling time constant $\tau_T = 1.0$ ps). In the first step of the simulation, we relax the conformation of MX branches with high temperature because the initial coordinates of MX chains often contain unrealistic frustrations. The system is simulated at 2000 K for 10⁷ steps (150 ns), which corresponds to the relaxation time of the end-to-end vector of the longer MX branch. Then, the system is cooled from 2000 K to typical room temperature (300 K) in steps of 50 K. We simulate 3 ns (2 × 10⁵ time steps) at each temperature and 7.5 ns (5 × 10⁵ time steps) more at 300 K. The system is further equilibrated for 7.5 ns (5 × 10⁵ time steps) under semi-isotropic pressure coupling (Berendsen coupling with time constant $\tau_p = 5.0$ ps and compressibility that is a control parameter of the strength of compression toward the target pressure 4.5 × 10⁻⁷ kPa⁻¹), where xy plane and z direction are independently controlled.

Production runs are performed under semi-isotropic pressure coupling. The systems are elongated from 0 to 2% in steps of 0.5% and from 2 to 5% in steps of 1% in fibril direction by manually rescaling L_z and all z coordinates to measure uniaxial tension. At each elongation, molecular dynamics is performed for 15 ns (1 × 10⁶ time steps) and the second half of the simulation is used for analysis. In this

stage, the compressibility of the Berendsen barostat in z (fibril) direction is set to 0.0 and L_z is kept fixed.

The system is also sheared to represent the three-point bending test of the real seta.⁷ In our simulation, we shear the xy plane (surface cross-sectional to fibril (z) axis) in x direction. We first shear systems under deformational shear velocity (1.0 × 10⁻⁵ nm ps⁻¹) during 5 ns (5 × 10⁵ time steps). The shear velocity is relatively small to relax the amorphous branches. This deformational velocity represents a shear rate of 5.2 × 10⁻⁷ ps⁻¹ for the seta model and 9.3 × 10⁻⁷ ps⁻¹ for the pure matrix. The time step is 0.01 ps, and the system is controlled by semi-isotropic NPT ensemble (Berendsen thermostat: 300 K and $\tau_T = 1.0$ ps; semi-isotropic Berendsen coupling for pressure: $\tau_p = 5.0$ ps; and compressibility: 0.0 and 4.5 × 10⁻⁷ kPa⁻¹ in xy plane and z direction, respectively) under Lees–Edwards (periodic) boundary condition.³⁵ Note: we use the shear machinery of Gromacs only to achieve a finite shear strain, not to simulate the system under constant shear load, as one would do for viscosity calculations. We halt the shearing process when a desired shear displacement has been reached. Then, we simulate for 10 ns (1 × 10⁶ time steps with 0.01 ps integration time) by fixing the rectangular system box. At this stage, anisotropic pressure coupling (Berendsen coupling with $\tau_p = 5.0$ ps, and the diagonal components of the compressibility are 4.5 × 10⁻⁷ kPa⁻¹, whereas the off-diagonal components are 0.0 kPa⁻¹) is selected to maintain the rectangular shape. The xz component of stress tensor is evaluated from the last half of the second stage. We consecutively repeat these two processes four times: the seta model is sheared from 0 to ca. 1% in steps of ca. 0.25%, whereas the pure matrix is sheared from 0 to ca. 2% in steps of ca. 0.5% over the whole production run.

5. RESULTS AND DISCUSSION

Poisson's ratios of both the seta model (MX and FB beads) and the pure matrix model (only MX beads) under strain from 0 to 5% are shown in Figure 4. They have been determined by stretching the system in the z direction (for the seta model, this is the fibril direction) and measuring the contraction of the x and y dimensions under semi-isotropic pressure coupling. Poisson's ratio depends little on the strain. The average value for the seta model is $\nu = 0.25 \pm 0.008$, and the one for the

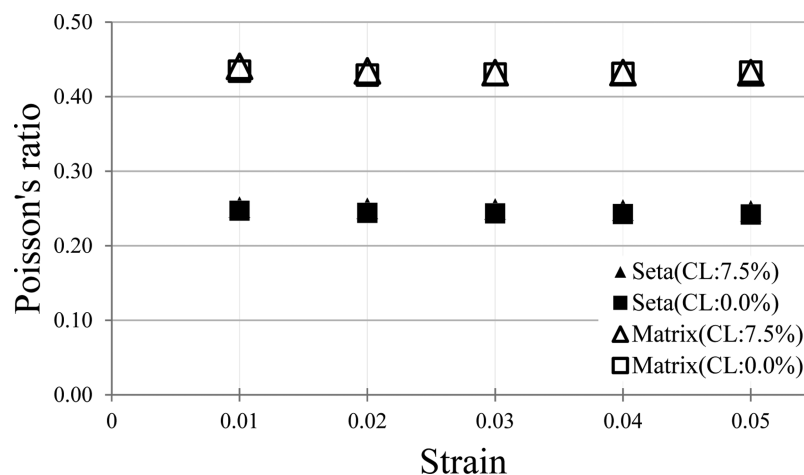


Figure 4. Poisson's ratio for the seta (fibril and matrix) system (full symbols) and for the pure matrix without fibrils (open symbols). Data are categorized by the amount of cross-links (CLs): data with 0% cross-links are triangles, and data with 7.5% cross-links are squares. The strain is applied in the direction of the fibrils.

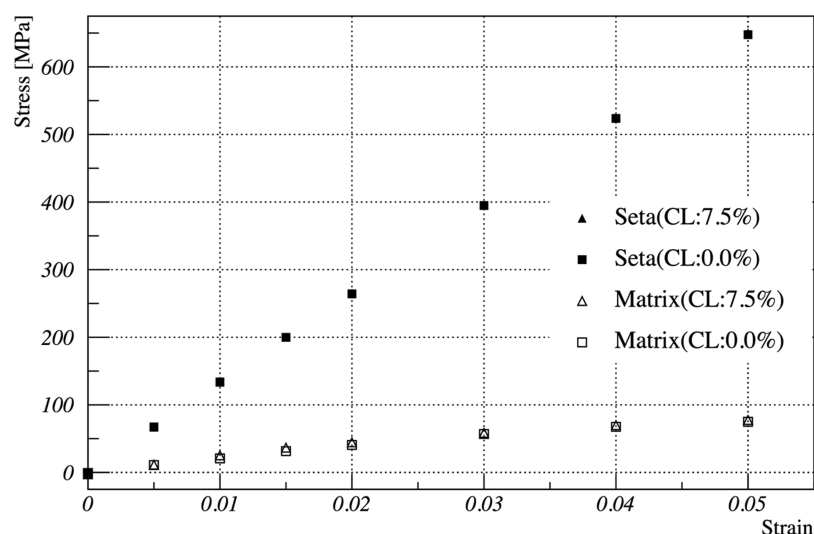


Figure 5. Stress–strain curve for the seta (fibril and matrix) system (full symbols) and for the pure matrix without fibrils (open symbols). Data are categorized by the amount of cross-links (CLs): data with 0% cross-links are triangles, and data with 7.5% cross-links are squares (overlapped with data in 0% cross-links). Young's moduli for the seta and matrix model are evaluated from the slope, and the values are 13.2 ± 0.02 and 2.13 ± 0.059 GPa, respectively. The values of the pure matrix are 1/6 less than those of the seta model. The curves bend from 3% strain onward. This effect is masked for the seta model because of the dominating stiffness of the fibril interactions. The cross-links density (triangles: 0% cross-links; squares: 7.5% cross-links) does not affect the results.

matrix model is $\nu = 0.43 \pm 0.007$, where the error indicates the standard error of the mean. The experimental range of Poisson's ratio for seta is 0.2–0.4,^{12,13,36,37} and our prediction is well within it.

The pure matrix is less compressible than the seta. The reasons for the lower Poisson's ratio of the seta model are: the fibrils restrict the conformation of the matrix region and they (FB beads occupy 36.6% of the cross section) do not change their cross sections in our model, so the transverse shrinking is lower. Of the cross-sectional area of our seta model, only about 63.4% is compressible matrix material. If we assume the matrix material to have the same Poisson ratio in the seta and in its pure form, and the fibril to be completely incompressible, we predict Poisson's ratio of the seta to be 0.27. This agrees well with the calculated value. The cross-links also restrict the movement of matrix chains. The difference of Poisson's ratio between no cross-links and a cross-link density of 7.5 is 2.5% at any given strain for the seta model, but not for the matrix model. The shift is comparable to that found in simulations of epoxy polymers, where Poisson's ratio changes 3%, when the system was changed from no cross-links to 5% cross-links.³⁸ Both cross-links and fibrils restrict the conformational freedom of matrix chains: looking at Poisson's ratio, we find the fibrils to be the more influential of the two.

The stress–strain curve along the fibril direction of the seta model is shown in full symbols in Figure 5. We extend to 6% strain, which is the strain at failure in experiments.^{7,11} Young's modulus is calculated from the slope of the curve to be 13.2 ± 0.02 GPa, where the fitting is performed from 0 to 2% strain because the curves start to tilt beyond 2%. This high modulus is due to the strong FB–FB interactions parallel to the fibrils. For reference, Young's modulus of the pure matrix system is 2.13 ± 0.059 GPa (open symbols, Figure 5), which is almost 1/6 that of the fibril–matrix system. This confirms that the matrix is much softer than fibril-enforced regions, which has also been observed in nature: for example, keratins of a soft-shell turtle's shell do not have the fibrils region (core-box) and the shell is actually softer (only qualitative description

available²⁵) than normal turtle shell (3.6 ± 1.5 GPa³⁹). Our estimate of the seta modulus exceeds the experimental values: data by Huber et al. (7.3 ± 1.0 GPa, Figure 2 in ref 7) are 25% less than our value, and the stress–strain curve by Prowse et al. (Figure 2 in ref 11) is about 1/4 of ours. The data by Huber et al. have been acquired in vacuum, namely, where the seta is stiffest. In contrast, the data by Prowse have been collected at 30% relative humidity, which leads to softening of keratin.¹¹ It, thus, seems that the presence of water can cause the seta to be much softer than in our calculation. Still, a discrepancy also remains for the dry seta.¹¹ A possible reason for the overestimation in our model may be a too ideal hexagonal packing of fibrils (Figure 1C) that would increase Young's modulus. In real setae, the fibrils may be less well ordered,^{1,4,23,40} which would also decrease their density per cross-sectional area and lead to a decrease of elastic modulus. In this sense, our prediction should be regarded as an ideal, upper limit of the stiffness in the fibril region. Another, more likely, reason is the composition of the measured system. The experiments were carried out on the central area of a seta, which contains both dense fibril area and light matrix area (Figure 4 in Rizzo et al.⁴ in cross section; Figure 5 in Huber et al.⁷ in fibril direction). Our model studies only the fibril area. Thus, it should be closer to the material of the spatula, which contains essentially no matrix regions.^{4,26} There are, however, no elasticity measurements available for spatulae to compare with. If we extract the fraction of matrix area from the cross section (Figure 4 by Rizzo et al.⁴), then we find that about 30% is pure matrix, which is consistent with the volume fraction of matrix material in the longitudinal direction ($31.2 \pm 4\%$ ⁷). If we assume Young's moduli to be additive and substitute our value of 2.1 GPa for the matrix area, we predict an overall Young's modulus of 0.3×2.1 GPa + 0.7×13.2 GPa $\times 0.7 = 9.7$ GPa, which is close to the vacuum measurement of 7.3 ± 1.0 GPa of Huber et al.⁷ If, as an extreme case, we were to assume the matrix to consist of lipids, as discussed by Alibardi,²⁶ with a Young's modulus of less than 100 MPa,⁴¹ the overall modulus would become 0.3×0.1 GPa + 0.7×13.2

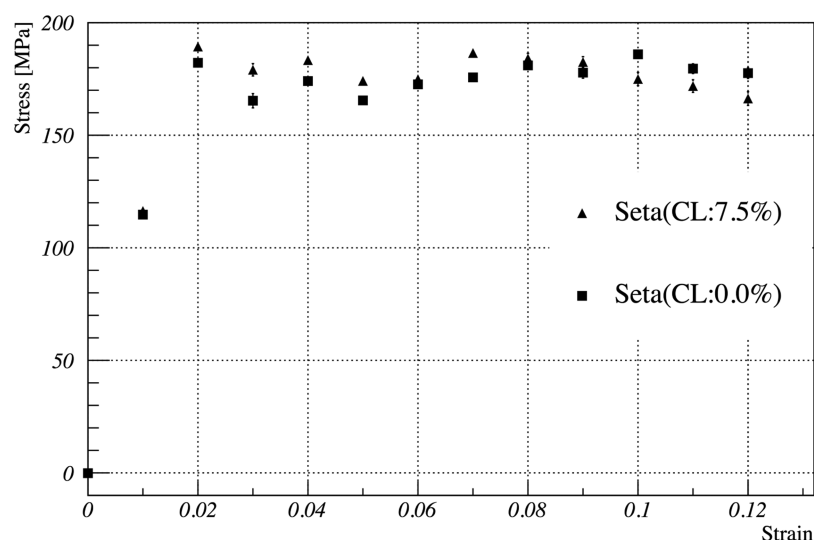


Figure 6. Seta model with a breakable FB–FB interaction along the fibrils. It shows a plateau in the stress–strain curve. This is comparable to experimental results at high humidity.

GPa = 9.2 GPa. As the amount of matrix materials decreases toward the end of the seta and into the spatulae, our predicted stiffness is probably more representative for a spatula, which contains almost no matrix region (Figure 3d in Rizzo et al.⁴).

The shear modulus of the pure matrix model is 0.80 ± 0.14 GPa. It is consistent with a shear modulus calculated from Young's modulus and Poisson's ratio $E/2(1 + \nu) = 0.74$ GPa. We thus confirm that the mechanical behavior of the matrix is isotropic. In contrast, the shear modulus for the seta model in bending direction (zx -component of stress tensor) is 0.52 ± 0.092 GPa. The value is close to that of the matrix model and hence indicates that the seta model bends like matrix. This enables a seta to bend easily when the gecko walks and tries to fit spatula optimally onto a wall. If we evaluate Young's modulus from the shear modulus and Poisson's ratio of the seta model, then it becomes $2G(1 + \nu) = 1.3$ GPa. This value is much different from the modulus from elongation simulations (12 GPa) because of the anisotropy of seta, but the value agrees well with the experimental Young's modulus from the bending experiment (1.7 ± 0.6 GPa⁷). If we consider again the volume fraction of the matrix and the fibril area, the additive value becomes 0.30×2.28 GPa + 0.70×1.30 GPa = 1.6 GPa, which is also consistent with the experimental value.⁷ Here, we use the value 2.28 GPa for Young's modulus of the matrix evaluated from the shear modulus. Our result shows that shear modulus of the seta model is close to that of the pure matrix and it reproduces the experimental results. Our fibril model thus shows a strong stiffness with respect to stretching, but not with respect to bending. The good agreement with experiment gives strong support to our parameterization approach that started from the interactions of individual amino acids.

Our model is probably too coarse-grained to study the effect of humidity directly, i.e., by the addition of disconnected small particles representing water. We can, however, implicitly account for its presence. The experimental stress–strain curves show that water decreases Young's modulus. They exhibit a plateau between 3 and 8% strain at 80% relative humidity (Figure 2 in Prowse et al.¹¹). Macroscopically, this is a brittle-to-ductile transition driven by water uptake. The slope of the stress–strain curve drops from 2.13 to 1.5 GPa beyond 10% strain, and the latter is consistent with the value of the pure

matrix phase. This entails that, at high water content, the fibrils stop conveying elasticity to the setae at large deformations. A possible molecular reason is that water breaks up the strong nonbonded interactions between consecutive β -sheet blocks along the fibril. We have put this hypothesis to the test using a breakable Lennard-Jones 12-6 potential for the FB–FB interaction such that their pair force becomes zero gradually (parameters: $\epsilon^{\text{FB-FB}} = 2\epsilon^{\text{FB-FB}'} = 268.4$ kJ mol⁻¹, $\sigma^{\text{FB}} = 0.456$ nm, and $r_0^{\text{FB-FB}} = 0.6884$ nm, instead of the use of the FB–FB harmonic bond in Table 1). The curve with the modified FB–FB potential is shown in Figure 6. From 2% strain onward, FB beads begin to separate (not shown) and the curves form a plateau. Thus, the specific weakening of intrafibrillar interactions is a plausible reason for the behavior observed experimentally under humidity rather than a nonspecific, uniform softening of all components.

6. CONCLUSIONS

We have constructed a coarse-grained molecular simulation model for β -keratin, which forms the setae and spatulae of gecko feet. This model is aimed at the elastic properties of this material. We regard keratin as a fiber-reinforced elastomer, which consists of amorphous matrix regions, into which fibrillar regions are embedded. The fibrillar regions themselves contain nanofibrils made of keratin β -sheets, hexagonally packed into their own amorphous matrix. We use a simplified description, which consists of two bead types. One represents entire amino acids as single sites and is used for all amorphous material of keratin, both outside and inside its fibrillar regions. It is the same for all amino acids, i.e., all sequence specificity is averaged out, but it does allow for cross-links (disulfide bonds). The second, much larger bead type encompasses whole dimers of β -sheet segments, which are considered to be rigid objects. Both bead types have been parameterized in a bottom-up fashion starting from the MARTINI force field.^{29–31} We note that adjustments have been made to match the density of the two keratin phases, but no other macroscopic experimental information has been used in the parameterization and, in particular, no elasticity data.

The model predicts Young's moduli of fibrillar and amorphous regions of setae to be 13.2 ± 0.02 and $2.13 \pm$

0.059 GPa, respectively. Adjusting for the experimentally observed volume fractions of amorphous (~ 0.3) and fibrillar regions (~ 0.7), we estimate Young's modulus of whole setae to be around 9.7 GPa, which is in reasonable agreement with the experimental data for dry setae (7.3 ± 1.0 GPa⁷). Similar agreement is found for Poisson's ratio. Shear moduli of fibrillar and amorphous regions are evaluated (0.52 ± 0.092 and 0.80 ± 0.14 GPa, respectively). Thus, a seta is much stiffer than the pure matrix in elongation, but bends in a similar manner to the pure matrix. Young's modulus evaluated from Poisson's ratio and the shear modulus of the fibrillar region (1.3 GPa) reproduce the experimental bending elasticity quite well (1.7 ± 0.6 GPa⁷). Breaking down the moduli into separate contributions from the amorphous matrix and the nanofibrils allows us to estimate them for other keratins or other conditions. For example, the model should also work for avian feathers, which have similar composition and morphology of their keratin to those of the gecko. Finally, we have selectively weakened the interactions between beads representing consecutive fibril segments, mimicking the breakup of these interactions by adsorbed water at high relative humidity. When this is done, the stress-strain curves of keratin change from a monotonous increase at all strains over to a plateau formation above 2% strain, which is also seen experimentally.¹¹ These results support the hypothesis that adsorbed water selectively undoes the strong adhesion between fibril segments so that stress has to be carried by the amorphous matrix, thereby dropping the modulus by an order of magnitude.

AUTHOR INFORMATION

Corresponding Author

*E-mail: k.endoh@theo.chemie.tu-darmstadt.de. Tel: +49-6151 16-22611. Fax: +49-6151 16-22619.

ORCID

Kenkoh S. Endoh: 0000-0002-3700-5222

Florian Müller-Plathe: 0000-0002-9111-7786

Notes

The authors declare no competing financial interest.

ACKNOWLEDGMENTS

The authors gratefully acknowledge fruitful discussions with Professor Stanislav Gorb, Kiel University. This work was supported in part by a fellowship from Honjo International Scholarship Foundation, GCOE Program "Weaving Science Web beyond Particle-Matter Hierarchy" by the Japan Society for the Promotion of Science (JSPS), and Grants-in Aid for Scientific Research (B) (Grant number: 26287096) from the Ministry of Education, Culture, Sports, Science and Technology, Japan.

REFERENCES

- (1) Federle, W. Why are so many adhesive pads hairy? *J. Exp. Biol.* **2006**, *209*, 2611–2621.
- (2) Arzt, E.; Gorb, S.; Spolenak, R. From micro to nano contacts in biological attachment devices. *Proc. Natl. Acad. Sci. U.S.A.* **2003**, *100*, 10603–10606.
- (3) Gorb, S. N. *Springer Handbook of Nanotechnology*; Bhushan, B., Ed.; Springer-Verlag: Berlin, 2010; pp 1525–1551.
- (4) Rizzo, N. W.; Gardner, K. H.; Walls, D. J.; Keiper-Hrynko, N. M.; Ganzke, T. S.; Hallahan, D. L. Characterization of the structure and composition of gecko adhesive setae. *J. R. Soc., Interface* **2006**, *3*, 441–451.
- (5) Autumn, K.; Majidi, C.; Groff, R. E.; Dittmore, A.; Fearing, R. Effective elastic modulus of isolated gecko setal arrays. *J. Exp. Biol.* **2006**, *209*, 3558–3568.
- (6) Autumn, K.; Peattie, A. M. Mechanisms of adhesion in geckos. *Integr. Comp. Biol.* **2002**, *42*, 1081–1090.
- (7) Huber, G.; Orso, S.; Spolenak, R.; Wegst, U. G. K.; Enders, S.; Gorb, S. N.; Arzt, E. Mechanical properties of a single gecko seta. *Int. J. Mater. Res.* **2008**, *99*, 1113–1118.
- (8) Autumn, K.; Sitti, M.; Liang, Y. A.; Peattie, A. M.; Hansen, W. R.; Sponberg, S.; Kenny, T. W.; Fearing, R.; Israelachvili, J. N.; Full, R. J. Evidence for van der Waals adhesion in gecko setae. *Proc. Natl. Acad. Sci. U.S.A.* **2002**, *99*, 12252–12256.
- (9) Loskill, P.; Puthoff, J.; Wilkinson, M.; Mecke, K.; Jacobs, K.; Autumn, K. Macroscale adhesion of gecko setae reflects nanoscale differences in subsurface composition. *J. R. Soc., Interface* **2013**, *10*, No. 20120587.
- (10) Tian, Y.; Pesika, N.; Zeng, H.; Rosenberg, K.; Zhao, B.; McGuiggan, P.; Autumn, K.; Israelachvili, J. Adhesion and friction in gecko toe attachment and detachment. *Proc. Natl. Acad. Sci. U.S.A.* **2006**, *103*, 19320–19325.
- (11) Prowse, M. S.; Wilkinson, M.; Puthoff, J. B.; Mayer, G.; Autumn, K. Effects of humidity on the mechanical properties of gecko setae. *Acta Biomater.* **2011**, *7*, 733–738.
- (12) Kim, T. W.; Bhushan, B. Effect of stiffness of multi-level hierarchical attachment system on adhesion enhancement. *Ultra-microscopy* **2007**, *107*, 902–912.
- (13) Sauer, R. A. Multiscale modeling and simulation of the deformation and adhesion of a single gecko seta. *Comput. Methods Biomech. Biomed. Eng.* **2009**, *12*, 627–640.
- (14) Gorb, S. N.; Filippov, A. E. Fibrillar adhesion with no clusterisation: Functional significance of material gradient along adhesive setae of insects. *Beilstein J. Nanotechnol.* **2014**, *5*, 837–845.
- (15) Bonser, R. H. C.; Purslow, P. P. The Young's-Modulus of feather keratin. *J. Exp. Biol.* **1995**, *198*, 1029–1033.
- (16) Feughelman, M. Natural protein fibers. *J. Appl. Polym. Sci.* **2002**, *83*, 489–507.
- (17) Akkermans, R. L. C.; Warren, P. B. Multiscale modelling of human hair. *Philos. Trans. R. Soc., A* **2004**, *362*, 1783–1793.
- (18) Qin, Z.; Buehler, M. J. Molecular dynamics simulation of the α -helix to β -sheet transition in coiled protein filaments: evidence for a critical filament length scale. *Phys. Rev. Lett.* **2010**, *104*, No. 198304.
- (19) Smith, T. A.; Parry, D. A. D. Three-dimensional modelling of interchain sequence similarities and differences in the coiled-coil segments of keratin intermediate filament heterodimers highlight features important in assembly. *J. Struct. Biol.* **2008**, *162*, 139–151.
- (20) Alibardi, L. Immunolocalization of specific keratin associated beta-proteins (beta-keratins) in the adhesive setae of Gekko gekko. *Tissue Cell* **2013**, *45*, 231–240.
- (21) Fraser, R. D. B.; Parry, D. A. D. Molecular packing in the feather keratin filament. *J. Struct. Biol.* **2008**, *162*, 1–13.
- (22) Fraser, R. D. B.; Parry, D. A. D. The role of β -sheets in the structure and assembly of keratins. *Biophys. Rev.* **2009**, *1*, 27–35.
- (23) Fraser, R. D. B.; MacRae, T. P.; Parry, D. A. D.; Suzuki, E. The structure of feather keratin. *Polymer* **1971**, *12*, 35–56.
- (24) Filshie, B. K.; Rogers, G. E. An electron microscope study of the fine structure of feather keratin. *J. Cell Biol.* **1962**, *13*, 1–12.
- (25) Toni, M.; Valle, L. D.; Alibardi, L. Hard (beta-) keratins in the epidermis of reptiles: composition, sequence, and molecular organization. *J. Proteome Res.* **2007**, *6*, 3377–3392.
- (26) Alibardi, L.; Edward, D. P.; Patil, L.; Bouhenni, R.; Dhinojwala, A.; Niewiarowski, P. H. Histochemical and ultrastructural analyses of adhesive setae of lizards indicate that they contain lipids in addition to keratins. *J. Morphol.* **2011**, *272*, 758–768.
- (27) Hallahan, D. L.; Keiper-Hrynko, N. M.; Shang, T. Q.; Ganzke, T. S.; Toni, M.; Valle, L. D.; Alibardi, L. Analysis of gene expression in gecko digital adhesive pads indicates significant production of cysteine- and glycine-rich beta-keratins. *J. Exp. Zool., Part B* **2009**, *312B*, 58–73.

- (28) Yin, N. E.; Kissinger, R. H.; Tolgyesi, W. S.; Cottington, E. M. The effect of fiber diameter on the cosmetic aspects of hair. *J. Soc. Cosmet. Chem.* **1977**, *28*, 139–150.
- (29) Marrink, S. J.; Risselada, H. J.; Yefimov, S.; Tielman, D. P.; de Vries, A. H. The MARTINI force field: coarse grained model for biomolecular simulations. *J. Phys. Chem. B* **2007**, *111*, 7812–7824.
- (30) Monticelli, L.; Kandasamy, S. K.; Periole, X.; Larson, R. G.; Tieleman, D. P.; Marrink, S. J. The MARTINI coarse-grained force field: extension to proteins. *J. Chem. Theory Comput.* **2008**, *4*, 819–834.
- (31) de Jong, D. H.; Singh, G.; Bennett, W. F. D.; Arnarez, C.; Wassenaar, T. A.; Schäfer, L. V.; Periole, X.; Tieleman, D. P.; Marrink, S. J. Improved parameters for the martini coarse-grained protein force field. *J. Chem. Theory Comput.* **2013**, *9*, 687–697.
- (32) Gautieri, A.; Russo, A.; Vesentini, S.; Redaelli, A.; Buehler, M. J. Coarse-grained model of collagen molecules using an extended martini force field. *J. Chem. Theory Comput.* **2010**, *6*, 1210–1218.
- (33) Wilson, R. H.; Lewis, H. B. The cystine content of hair and other epidermal tissues. *J. Biol. Chem.* **1927**, *73*, 543–553.
- (34) Fischer, H.; Polikarpov, I.; Craievich, A. F. Average protein density is a molecular-weight-dependent function. *Protein Sci.* **2004**, *13*, 2825–2828.
- (35) Lees, A. W.; Edwards, S. F. The computer study of transport processes under extreme conditions. *J. Phys. C: Solid State Phys.* **1972**, *5*, 1921.
- (36) Gao, H.; Wang, X.; Yao, H.; Gorb, S.; Arzt, E. Mechanics of hierarchical adhesion structures of geckos. *Mech. Mater.* **2005**, *37*, 275–285.
- (37) Greiner, C.; del Campo, A.; Arzt, E. Adhesion of bioinspired micropatterned surfaces: effects of pillar radius, aspect ratio, and preload. *Langmuir* **2007**, *23*, 3495–3502.
- (38) Shokuhfar, A.; Arab, B. The effect of cross linking density on the mechanical properties and structure of the epoxy polymers: molecular dynamics simulation. *J. Mol. Model.* **2013**, *19*, 3719–3731.
- (39) Achrai, B.; Wagner, D. Micro-structure and mechanical properties of the turtle carapace as a biological composite shield. *Acta Biomater.* **2013**, *9*, 5890–5902.
- (40) Cameron, G. J.; Wess, T. J.; Bonser, R. H. C. Young's modulus varies with differential orientation of keratin in feathers. *J. Struct. Biol.* **2003**, *143*, 118–123.
- (41) Picas, L.; Rico, F.; Scheuring, S. Direct measurement of the mechanical properties of lipid phases in supported bilayers. *Biophys. J.* **2012**, *102*, L01–L03.